Spatial characterization of near-surface structure and meltwater runoff conditions across Devon Ice Cap from dual-frequency radar reflectivity

Kristian Chan[1], Cyril Grima[1], Anja Rutishauser[2], Duncan A. Young[1], Riley Culberg[3], Donald D. Blankenship[1]

[1]Institute for Geophysics, University of Texas at Austin, Austin, TX, 78758, USA
[2]Geological Survey of Denmark and Greenland, Copenhagen, Denmark
[3]Department of Electrical Engineering, Stanford University, Stanford, CA, 94305, USA

Correspondence to: Kristian Chan (kristian.chan@utexas.edu)

Abstract. Melting and refreezing processes in the firn of Devon Ice Cap control meltwater infiltration and runoff across the ice cap, but their full spatial extent and effect on near-surface structure is difficult to measure with ground-based traverses or existing satellite remote sensing. Here, we derive the coherent component of the near-surface return from airborne ice-penetrating radar over Devon Ice Cap, Canadian Arctic, to characterize firn containing centimeter to meter-thick ice layers (i.e., ice slabs) formed from refrozen meltwater in firn. Comparison with reflectivities using a thin layer reflectivity model, informed by ground-based radar and firn core measurements, indicate that the coherent component is sensitive to the near-surface firn structure composed of quasi-specular ice and firn layers, limited by the bandwidth-constrained radar range resolution. By leveraging their differences in range resolution, we assess the use of dual-frequency airborne ice-penetrating radar to characterize the spatial and vertical near-surface structure of Devon Ice Cap. Our results suggest that average ice slab thickness throughout the Devon Ice Cap percolation zone ranges from 4.2 to 5.6 m. This implies conditions that can enable lateral meltwater runoff and potentially contribute to the total surface runoff routed through supraglacial rivers down glacier. Together with the incoherent component of the surface return previously studied, our dual-frequency approach provides an alternative method for characterizing bulk firn properties, particularly where ground-based and higher frequency radar data are not available.

1 Introduction

Over the past several decades, the threat of sea level rise has led to increased attention on how Earth's polar regions respond to climate change. Warmer temperatures have led to increasing surface meltwater on glaciers and ice sheets in the Arctic (Mortimer et al., 2016; Trusel et al., 2018). However, the contribution of surface meltwater runoff to surface mass balance is complicated by the potential of meltwater refreezing in firn with sufficient cold content (i.e., the energy required to bring firn to its melting temperature), thereby buffering mass loss (van den Broeke et al., 2016; MacFerrin et al., 2019; Vandecrux et al., 2020a). The processes governing melting and refreezing are complex and remain challenging to capture in firn models,

which yield large discrepancies between estimates of meltwater retention (Vandecrux et al., 2020b). For example, refreezing releases latent heat, which subsequently induces local changes in temperature, thermal conductivity, and porosity in the firn column (Bezeau et al., 2013; van den Broeke et al., 2016). Meltwater that refreezes within the firn pore space typically form ice layers ranging from <0.1 m thick 'ice lenses' to meters-thick 'ice slabs' perched just below the surface (MacFerrin et al.,

35   2019). While firn remains relatively permeable in the presence of discontinuous thin ice lenses, the aggregation of ice lenses into horizontally continuous, low-permeability ice slabs over multiple seasons could in effect limit vertical meltwater percolation, thus promoting lateral runoff that could further contribute to sea level rise (Machguth et al., 2016; MacFerrin et al., 2019). Therefore, characterizing the effects of surface meltwater infiltration and refreezing on the firn's storage capacity is crucial for predicting the future runoff budget in response to increased climate warming.

40

Field-based techniques have expanded our knowledge of melting and refreezing processes in firn (Bell et al., 2008; Sylvestre et al., 2013; Forster et al., 2014; Gascon et al., 2014; Machguth et al., 2016), and their observations are necessary to help validate firn models that are often relied upon for mass balance estimates (Ashmore et al., 2020). Field studies typically utilize some combination of firn cores, snow pits, and ground-based radar (GPR) measurements, which provide in-situ

45   measurements or high resolution remotely sensed observations of the local firn column. However, such methods often lack the capability to study spatially extensive regions or ones difficult to access. Thus, surveys with large spatial coverage are especially important for characterizing the spatial extent of melting and refreezing processes in firn.

Airborne ice-penetrating radar surveys conducted at ultra high frequency (UHF) and higher have successfully mapped melt

50   layers and ice slabs in firn with extensive spatial coverage compared to ground-based methods (Arnold et al., 2019; MacFerrin et al., 2019; Culberg et al., 2021). However, most airborne ice-penetrating radars operate at VHF frequencies (hereinafter referred to only as IPR) and have commensurately lower bandwidths that limit their ability to resolve layers in the firn that are thinner than the radar range resolution (typically about 5-10 m, see Sec. 2.1) (Arnold et al., 2018). Despite these challenges, IPR has been successfully used to characterize near-surface properties (Rutishauser et al., 2016; Grima et

55   al., 2014b, 2016, 2019) and can be of benefit in regions lacking higher frequency radar coverage. Similar studies conducted at even lower frequencies have been used to study near-surface properties on Mars (Mouginot et al., 2009; Grima et al., 2012). Thus, such methods would be useful for interpreting data from future earth observing and planetary missions equipped with radar sounders.

60   Here, we apply the Radar Statistical Reconnaissance (RSR) method (Grima et al., 2014a) to IPR datasets collected over DIC including the Operation Ice Bridge (MacGregor et al., 2021) and the SEARCH^{Arctic} (SRH1) project (Rutishauser et al., 2022) as well as the initial 2014 (GOG3) survey (Rutishauser et al., 2018, 2016). RSR is a statistical method that links the distribution of surface echo amplitudes to an analytical probability density function in order to derive the coherent and incoherent components of the total surface power. We compare the coherent power to modeled reflectivity values using a

65 thin layer reflectivity model (Born and Wolf, 1970) along a profile with collocated GPR data, to assess coherent power sensitivity to near-surface structure. Although IPR cannot resolve layers thinner than the radar range resolution, we show how they can still modulate the surface coherent power. Rutishauser et al. (2016) previously used the incoherent surface power derived from the sparse GOG3 survey to map firn zones over DIC. These zones are distinguished by the presence of thin ice lenses (Zone I), thick ice slabs (Zone II), and predominantly compact ice (Zone III). In this study, we use the ratio of

70 the coherent to incoherent power to redefine these zones, derived from the SRH1 dataset providing greater spatial coverage compared to the GOG3 survey (Fig. 1). We also evaluate the use of a dual-frequency/bandwidth IPR approach for characterizing the vertical and spatial near-surface structure, both locally by zone and holistically across the ice cap. Finally, hypotheses about the near-surface hydrological conditions across zones are discussed based on our interpretations of the IPR data, supported by imagery on DIC.
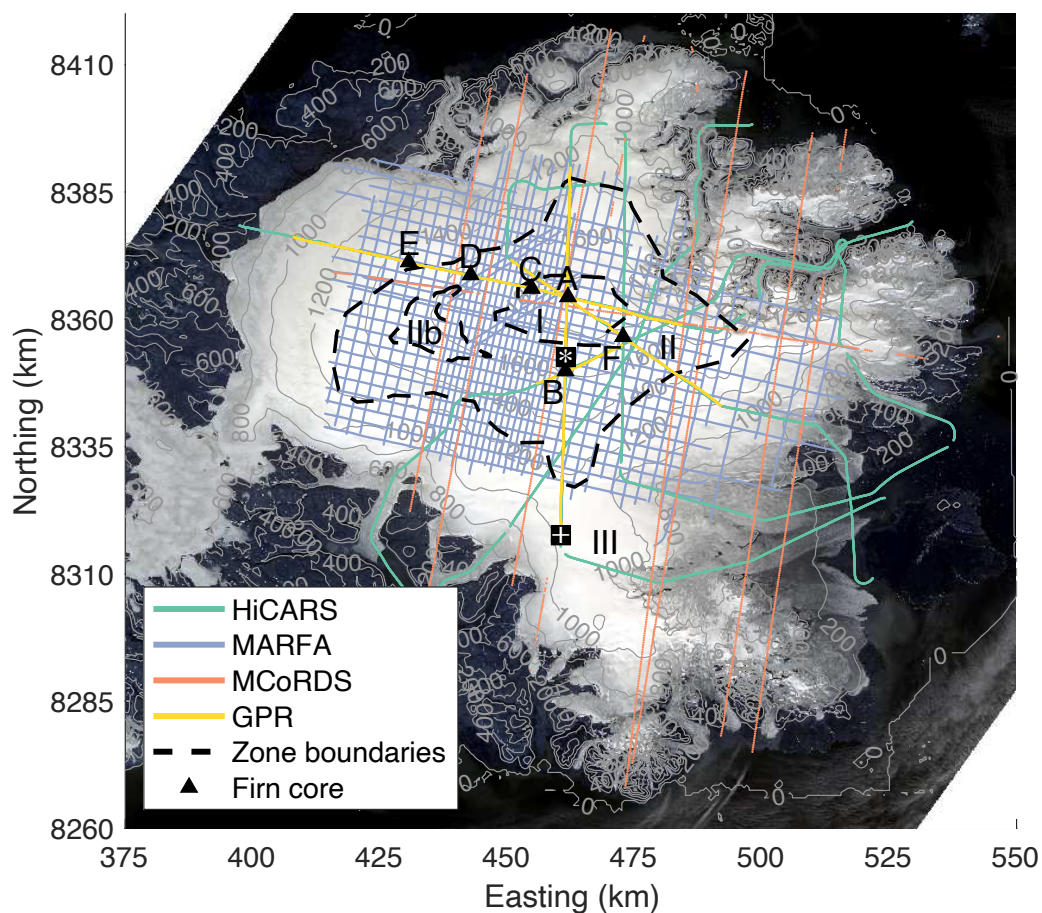
75

Figure 1. Map of airborne IPR data (HiCARS in 2014, MARFA in 2018, and MCoRDS in 2019) and GPR data (in 2015) collected over Devon Ice Cap. Firn zones are marked with roman numerals. The segment from '*' to '+' indicates the profile in Figure 2.

3

2 Data and Methods

2.1 Airborne ice-penetrating radar

80   IPR data were collected over DIC in 2014 with the High-Capability Airborne Radar Sounder 2 (HiCARS) (Peters et al., 2007; Rutishauser et al., 2016, 2018) and in 2018 with the Multifrequency Airborne Radar-sounder for Full-phase Assessment (MARFA) (Scanlan et al., 2020; Rutishauser et al., 2022), which is a dual-phase version of the HiCARS system (Fig. 1). Both instruments, operated by the University of Texas Institute for Geophysics, transmit a chirp with a center frequency (f_c) of 60 MHz and bandwidth of 15 MHz. In addition, IPR data collected by the University of Kansas

85   Multichannel Coherent Radar Depth Sounder 3 (MCoRDS) in 2019 was used for this study (Fig. 1), at a center frequency of 195 MHz and bandwidth of 30 MHz (MacGregor et al., 2021; Rodriguez-Morales et al., 2014).

The surface radar return is limited to a depth that is equal to the vertical/range resolution, which we can also refer to as the near-surface depth z_0. The range resolution, and thus z_0, is calculated as (Cavitte et al., 2021)

90

$$z_0 = \frac{kc}{2B\sqrt{\varepsilon_{eff}}},$$ (1)

where B is the radar bandwidth, c is the speed of light in vacuum, k is the windowing factor, and ε_{eff} is the effective permittivity of the target medium (Table 1). For MCoRDS, $k = 1.53$ as a result of the 20% Tukey time-domain window and

95   Hanning frequency-domain window applied when performing pulse compression (CReSIS, 2016). For HiCARS/MARFA, we adopt a factor of $k = 1.515$, as the ratio of the 100 ns compressed pulse width used in practice (Cavitte et al., 2021) to the theoretical 66 ns obtained from the 15 MHz bandwidth. The effective permittivity of the near-surface is defined as a single permittivity derived from the permittivity of the individual components of a multi-component heterogeneous medium (Sihvola, 1999). For a homogeneous medium, the effective permittivity is simply the single value for that medium. However,

100   for a heterogeneous medium, the effective permittivity is usually unknown, because it is governed by various material properties, such as inclusion geometry, density, and impurities (Sihvola, 1999; Pettinelli et al., 2015). To partially account for this uncertainty, a layered medium can be used to represent the near-surface with prescribed layer thicknesses and permittivities (see Sec 2.3). Due to differences in B, the apparent surface echo observed by each radar system probes the near-surface to different depths, and the associated ε_{eff} is characteristic of the near-surface properties spanning that depth.

105

Radar System	f_c (MHz)	B (MHz)	ε_{eff}	z_0 (m)
HiCARS & MARFA	60	15	1.8	11.3
			3.15	8.5
MCoRDS	195	30	1.8	5.7
			3.15	4.3

110 **Table 1. Near-surface depth (i.e., range resolution) calculated with Eq. (1), for ice-penetrating radars used in this study. Selected permittivities are representative of a medium composed entirely of firn (1.8) and ice (3.15).**

We apply the Radar Statistical Reconnaissance (RSR) method to all IPR datasets in this study. In the RSR technique, a Homodyne K-distribution is fit to surface radar amplitudes over a specified along-track window, to deconvolve the signal into its coherent/specular (P_c) and incoherent/scattered (P_n) components (Grima et al., 2014a). Surface power was corrected
115 for geometric spreading loss to account for variations in aircraft altitude. For MCoRDS, a window of 5000 samples (equivalent to ~1.5 km) with a step size of 1250 samples was used, providing about 75% overlap. For both HiCARS and MARFA, a window of 1000 samples (equivalent to ~1 km) with a step size of 250 samples was used, also providing about 75% overlap.

120 P_c is mainly sensitive to the permittivity, which is governed by the near-surface composition and structure (e.g., layers). On the other hand, P_n is mainly sensitive to the surface roughness and random non-stratigraphic heterogeneities (e.g., voids) within the near-surface. In this work, we focus on P_c to constrain the thickness of ice layers in Zone II of the DIC firn. P_c can be further described as (Ulaby et al., 1981)

125 $$P_c = r^2 e^{-(2k\sigma_h)^2},$$ (2)

where r is the effective surface reflection coefficient, σ_h is the root mean square (RMS) height, and k is the wavenumber. Although P_c is a function of the RMS height, surface roughness is not the main contributor to surface scattering over DIC (Rutishauser et al., 2016). Therefore, we hypothesize that P_c will be predominantly sensitive to r^2 as opposed to surface
130 roughness. The DIC firn provides the opportunity to study how P_c varies with changes in the coherent near-surface structure/geometry through the various interferences between the reflections arising from the dielectric interfaces making up the firn/ice stack.

For this work, we focus on relative variations in coherent power between all surveys; thus, absolute calibration of the signal
135 is not necessary, although coherent power from the HiCARS survey was previously calibrated as noted in Rutishauser et al. (2016). Additionally, to ensure the underlying assumptions for RSR are met, data with a correlation coefficient (a goodness-of-fit estimator for the RSR technique) below 95% and an aircraft roll above 2.9° are excluded from the analysis. Previous

The Cryosphere
Discussions

applications of the RSR method have empirically shown that an aircraft roll of 2 to 3° allows for a stable coherent radar return. Data at elevations below 800 m are also excluded to remove observations collected over rock outcrops.

2.2 Ground-penetrating radar (GPR) and firn cores

We use ground-penetrating radar (GPR) data and firn cores to serve as ground-truth to interpret IPR observations over DIC. GPR surveys were conducted in spring 2015 collocated with several HiCARS transects (Fig. 1). Details of the GPR system and post-processing steps can be found in Rutishauser et al. (2016). We use the GPR data along the profile marked in Fig. 1 that traverses Zones II and III. Here, we identify an ice slab in the firn, and its thickness is used as an input to a thin layer reflectivity model (described below). The ice slab was obtained from manually picking the GPR radargram (Fig. 2b). Although the top of the ice slab is easily distinguishable in the radargram, the bottom of the ice slab is highly uncertain in several locations. Therefore, the bottom of the ice slab was picked as the first continuous reflection indicating an ice-firn transition as best as possible. Firn cores were collected along the GPR profiles during the same survey in spring 2015 (Fig. 1) (Rutishauser et al., 2016). Sections of the firn cores were used to derive the background/dry firn density (where no ice layers were present) at various depths (Fig. S1). The average density measurement error is estimated to be around 50 kg m^{-3}; however, we observe a few obvious outliers that we do not use in our analysis (Fig. S1).

2.3 Model description

The observed IPR surface power is the sum of all electric fields reflected and scattered due to dielectric contrasts within the range resolution and bounded spatially by the pulse-limited footprint (Grima et al., 2014a). As such, the observed power is expected to be modulated by near-surface properties (e.g., layers). Following previous studies, we model the reflection of electromagnetic radiation from a medium consisting of porous and compact ice layers (Mouginot et al., 2009; Grima et al., 2014b). The model is based on the transfer-matrix implementation, describing the interaction of an electromagnetic wave with a stratified medium consisting of homogeneous layers (Born and Wolf, 1970). More specifically, individual propagation matrices are generated with an assigned permittivity for each layer and an assigned thickness for all but the uppermost and bottommost layers in the stack. The product of these propagation matrices forms the characteristic matrix for the entire stack. The reflection coefficient r^2 for the medium can then be obtained from this characteristic matrix.

We model the reflectivity of stratified layers over DIC from HiCARS, using both 3-layer and 4-layer stack configurations (Fig. 2c). In this work, we refer to the porous ice layer above and below the ice slab as the firn$_1$ and firn$_2$ layer (when applicable), respectively. Values obtained from in-situ measured firn densities (Fig. S1) were converted to permittivities using an empirical model relating firn/ice density (ρ [kg m^{-3}]) to permittivity (ε) (Kovacs et al., 1995), calculated as

$$\varepsilon = (1 + 0.000845\rho)^2 \ . \tag{3}$$

170 Using Eq. (3), $\varepsilon = 1.8$ was obtained from $\rho = 417$ kg m^{-3} ± 40 kg m^{-3} for firn$_1$, by averaging firn core density measurements taken from the surface to 1 m depth. Similarly, $\varepsilon = 2.2$ was obtained from $\rho = 584$ kg m^{-3} ± 56 kg m^{-3} for firn$_2$, by averaging firn core density measurements taken between 2.5 and 11 m depths, excluding the two outliers with densities greater than that of compact ice (Fig. S1). $\varepsilon = 3.15$ was assigned to the ice slab (Fujita et al., 2000). For simplicity, we assign these bulk densities/permittivities to the firn layers in our model but acknowledge that the firn density is expected to vary horizontally

175 and vertically over the DIC near-surface.

The model does not account for surface roughness, of which effects on P_c are assumed to be negligible over DIC (Rutishauser et al., 2016). The model also does not account for relatively small-scale heterogeneities, such as residual firn embedded within a compact ice layer, and ice lenses embedded in the firn$_1$ and firn$_2$ layers. We discuss the implications of

180 these assumptions in the following section.

The HiCARS chirp is not monochromatic. Therefore, to consider the effects of all frequencies defined by the chirp's center frequency and bandwidth, we model the reflectivity from a particular stack configuration (R_N) as (Mouginot et al., 2009)

185 $$R_N = max(||IFFT(S(f)r(f,\delta z_{1...N},\varepsilon_{1...N})S^*(f))||^2),$$ (4)

where f is the frequency, S is the linearly modulated chirp in the frequency domain, N denotes the number of layers considered in the model, δz is the thickness of a particular layer, and ε is the permittivity of that layer in the stack configuration. A synthetic chirp was generated to represent S for HiCARS in this study, using a pulse length of 1 μs, 50

190 MHz sampling rate, and 1200 samples. The same sampling interval for S and r were used over the system bandwidth.

3 Results

3.1 Coherent power sensitivity to heterogenous near-surface structure
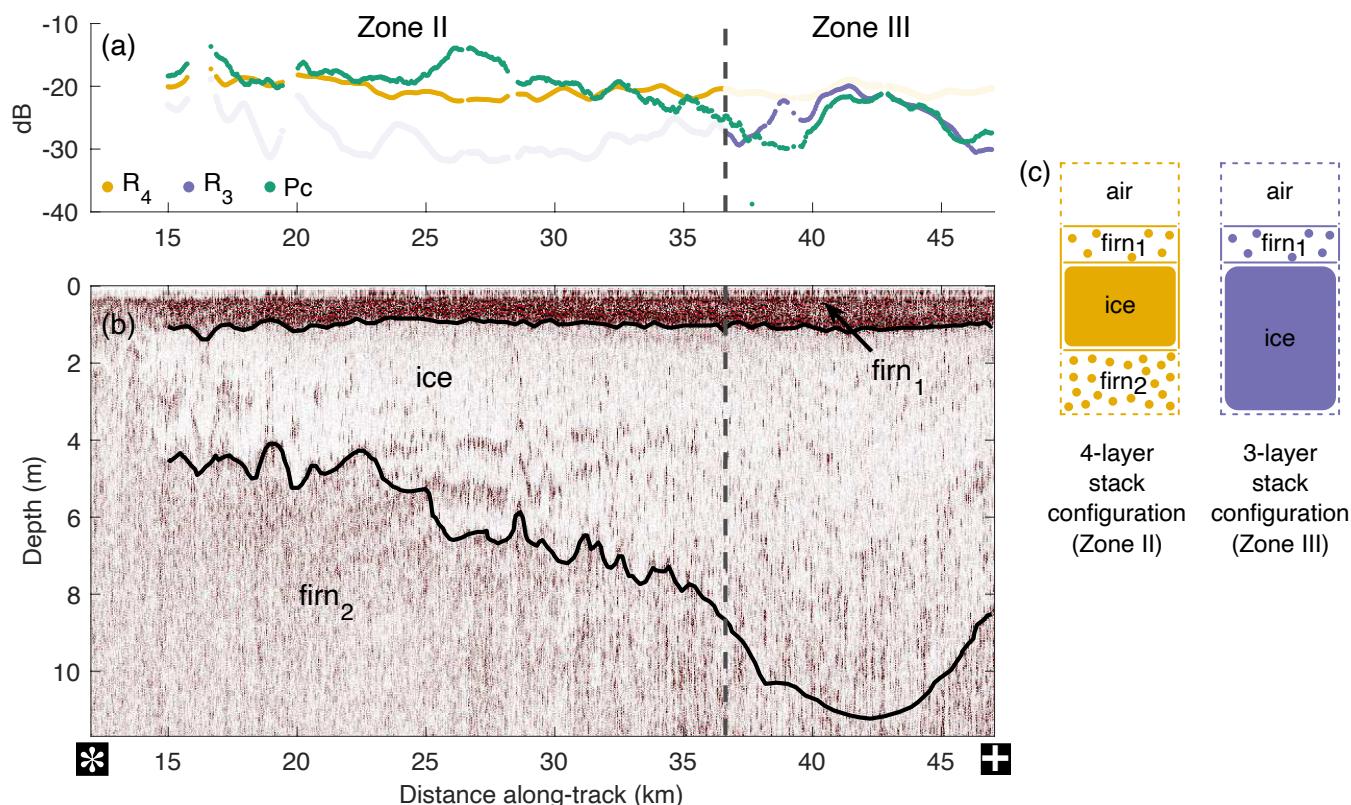
Figure 2. (a) HiCARS surface coherent power (P_c) along the segment from '*' to '+' of transect NDEVON/JKB2k/Y4a in Figure 1
and modeled reflectivity from 3-layer (R_3) and 4-layer (R_4) stack configurations. (b) GPR radargram along the same segment,
adapted from Rutishauser et al. (2016), with the Zone II to III boundary marked by the vertical black dashed line. Ice-firn
transitions were manually picked along this profile (black solid lines). (c) Graphical representation of the 3-layer and 4-layer stack
configurations used in the reflectivity model.

To understand how the vertical firn structure over DIC influences P_c, we compare modeled reflectivity R_N (where N indicates the stack configuration) to previously absolutely calibrated P_c derived from HiCARS (Rutishauser et al., 2016) along a transect with collocated GPR observations (Fig. 2). Between the two stack configurations represented in our model (Fig. 2c), there is better agreement between R_4 (4-layer stack) and P_c from about 15 to 35 km along-track in Zone II. In contrast, R_3 (3-layer stack) better approximates P_c from about 37 to 47 km along-track in Zone III. The shift from R_4 to R_3 occurs at the Zone II/III boundary, where the picked bottom ice slab interface (i.e., the ice-firn$_2$ interface) lies ~9 m beneath the surface (Fig. 2b). This depth coincides with the theoretical range resolution (Table 1) and thus also represents the apparent range resolution of HiCARS. While our model does not take into account range resolution constraints and integrates all coherent reflections picked from the GPR data, we find that it adequately predicts P_c along the profile best described by a stack configuration characteristic of the near-surface stratigraphy. Only near-surface coherent reflections

generated within the range resolution contribute to P_c. This implies that the reflection from the ice-firn$_2$ interface is

210 integrated into P_c in Zone II but not in Zone III. Our interpretation of P_c is consistent with the transition from embedded ice layers in the firn of Zone II to the mostly compact glacier ice of Zone III (Gascon et al., 2013; Rutishauser et al., 2016). Accordingly, the lower ice slab interface was picked to reside at depths well below the expected HiCARS range resolution in Zone III (F 2b).

215 Consideration of uncertainties in our model from measured firn densities yield reflectivity variations ranging from 1.5 to 2.9 dB, which can explain the slight offset between R_N and P_c but are still smaller than the full range of P_c values observed (~15 dB) along this profile. Differences between R_N and P_c could also be attributed to smaller inhomogeneities within the ice slab and firn layers. For example, interstitial firn can be seen within the ice slab from 15 to 18 km and from 25 to 28 km along the profile (Fig. 2b) but is not represented in our model. Such layers can likely generate additional reflections that could

220 constructively interfere and thus explain why P_c exceeds R_4 in those parts of the profile. We also do not account for ice lenses (cm-scale) in the firn$_1$ and firn$_2$ layers. Modeling of HiCARS surface reflectivity from an ice lens in firn accounts for <1 dB relative to a firn column without an ice lens (Fig. S2), although the presence of multiple ice lenses may have non-negligible effects. Uncertainties due to our manual picks were considered and shown in Fig. S3, by varying the pick of the lower ice slab interface. Results indicate minimal changes to modeled reflectivity values and cannot resolve the

225 discrepancies between R_4 and P_c, which further indicates our model is too simplistic to account for smaller complexities (i.e., multiple ice-firn transitions) that arise from heterogeneous melting and refreezing processes in firn. In light of the uncertainties responsible for mismatches between the modeled and observed values, our results indicate that the near-surface heterogeneous structure featuring an ice slab governs P_c from HiCARS to a first-order, when coherent reflections are generated within the HiCARS range resolution.

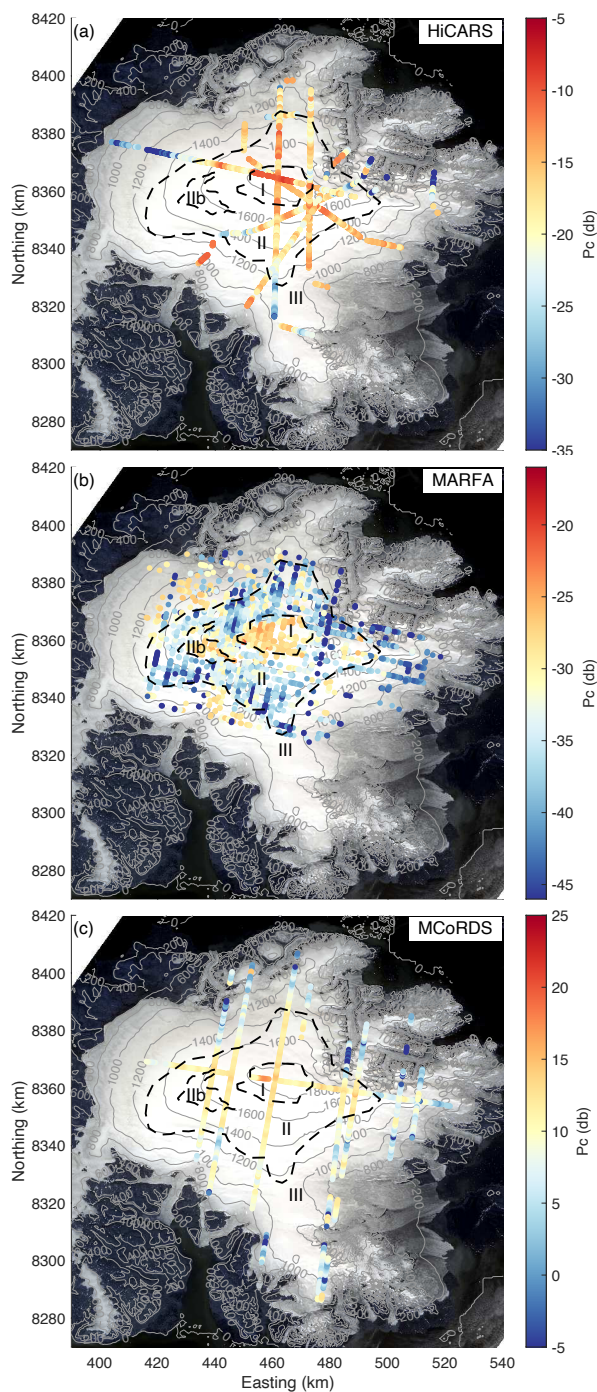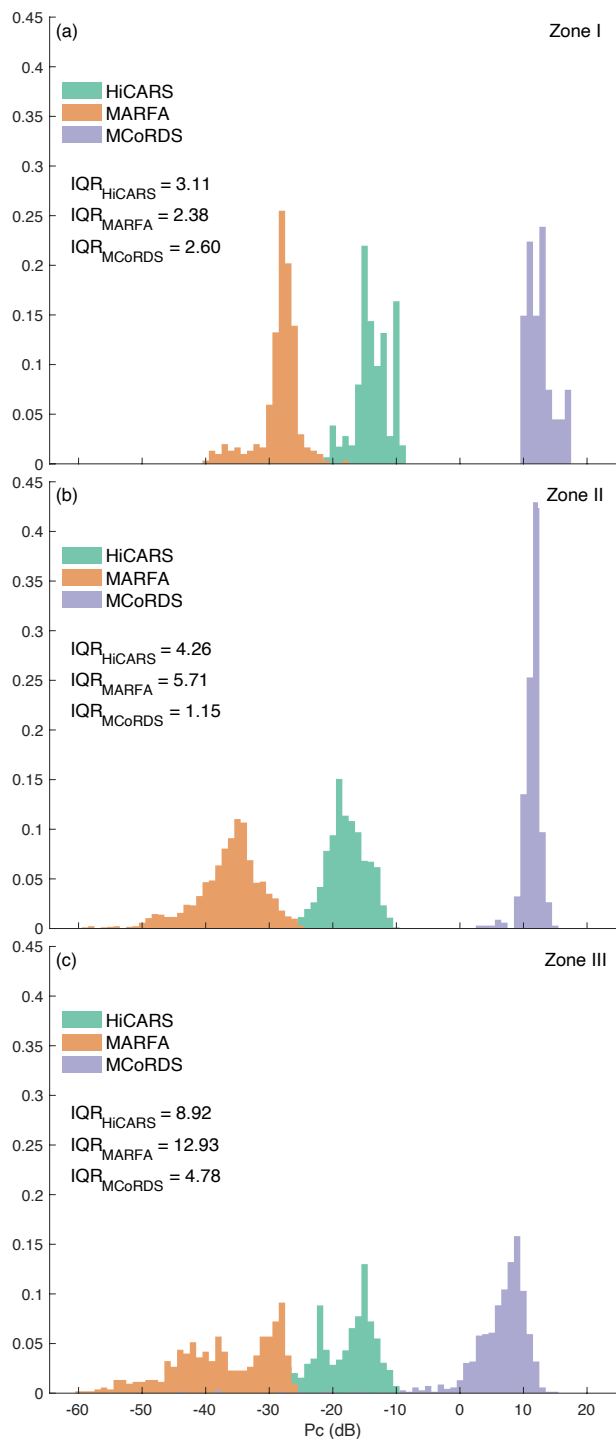## 3.2 Dual-frequency characterization approach of near-surface structure

Figure 3. Maps of surface coherent power (P_c) over Devon Ice Cap derived from IPR data collected with (a) HiCARS, (b) MARFA and (c) MCoRDS, all scaled to the same dynamic range to facilitate comparison between the surveys. Black dashed lines denote zone boundaries.

235

Figure 4. Normalized histogram distributions of P_c over Devon Ice Cap across (a) Zone I, (b) Zone II and (c) Zone III, by IPR survey and their corresponding interquartile ranges.

11

The Cryosphere
Discussions

Open Access

EGU

Differences in range resolution between two IPRs, operating at different frequencies and bandwidths, can be used to
240   investigate bulk properties of the near-surface (Chan, 2022). This approach is useful in the absence of data capable of
resolving the near-surface stratigraphy (e.g., firn cores, GPR or high-frequency airborne ice-penetrating radar). Here, we
analyze P_c derived from HiCARS/MARFA and MCoRDS to evaluate this approach (Fig. 3). We calculate the interquartile
range (IQR) of P_c distributions for each survey as a measure of P_c variability within each zone (Fig. 4).

3.2.1 Updated firn zone boundaries

245   Prior to conducting the dual-frequency analysis, firn zone boundaries previously identified in Rutishauser et al. (2016) were
updated using a similar method with the more recent MARFA survey. Rutishauser et al. (2016) previously hypothesized that
ice slabs in firn cause increased scattering of the radar return relative to thin ice lenses or glacial ice. We use the P_c/P_n ratio
as an indicator of relative scattering from the near-surface that excludes the effects of permittivity (Grima et al., 2014a). Firn
zone boundaries were refined based on visual inspection, such that Zone II consists of values where $P_c/P_n < 0$ dB (i.e., P_n
250   dominating), whereas Zones I and III consist of values where $P_c/P_n > 0$ dB (i.e., P_c dominating) (Fig. S4). The largest
discrepancy between the old and new boundaries occurs in the northwest part of DIC, where the new Zone II/III boundary
has migrated to higher elevations. When compared with LandSat-8 images taken in August 2019 (late into the melt season),
we observe that the new Zone II/III boundary is in good agreement with a transition from snow/firn to exposed bare
ice/meltwater (see Discussion). The images validate the lack of firn in the northwest part of DIC. We find that this method
255   for delineating firn zones is valid and advantageous, because it is also sensitive to bulk changes in the firn stratigraphy
between Zones I and II otherwise invisible to optical imagery.

3.2.2 Zone I: thin ice lenses in firn

Visual inspection of P_c observed across all three surveys within Zone I indicate their overall similar character (Fig. 3). IQRs
within Zone I are low, indicative of relatively less variability in P_c (Fig. 4). Interzonally, consistently high P_c values are also
260   observed for all three IPRs in Zone I compared to the other two zones by IPR survey. Altogether, these observations suggest
the bulk firn structure observed in Zone I appears similar to all IPRs, spatially and vertically, to depths bounded by the range
resolutions of each system. The firn in Zone I is known to host thin, flat ice lenses (Rutishauser et al., 2016), which can
generate coherent radar reflections. Firn cores collected in Zone I confirm the existence of ice lenses from the surface to ~11
m, which is also the depth approximately equivalent to the theoretical range resolution of HiCARS/MARFA (Table 1).
265   While MCoRDS is expected to be more sensitive to ice lenses than HiCARS/MARFA, owing to its higher frequency, the
integration of coherent reflections from multiple ice lenses at depths within the range resolution of each IPR could be
responsible for the high P_c values observed in Zone I across all three surveys.

12

3.2.3 Zone II: thick ice slabs in firn

P_c values from MCoRDS appear stable across the Zone I/II boundary (Fig. 3). However, a change in the pattern of P_c is
270 observed for HiCARS/MARFA between Zones I and II (Fig. 3), indicative of a change in the bulk near-surface firn structure
that primarily affects the 60 MHz IPR's coherent response. Within Zone II, IQRs of P_c from both HiCARS and MARFA are
more than three times greater than MCoRDS (Fig. 4b). HiCARS and MARFA operate with the same range resolution and
thus are expected to observe the firn column to the same depth, despite the surveys being conducted in different years.
MCoRDS operates with a finer range resolution and thus probes the firn to shallower depths.

275

In Zone II, we attribute differences in P_c variability between HiCARS/MARFA and MCoRDS to changes in the near-surface
firn properties to different depths, limited by each IPR's range resolution. Zone II is known to host meters-thick ice slabs in
the top 10 m of the firn column, in addition to thin ice lenses embedded in the firn (Gascon et al., 2013; Rutishauser et al.,
2016). The larger range resolution of HiCARS/MARFA indicates that P_c is affected by features in the firn column at depths
280 beyond the range resolution of MCoRDS, with the main feature being the bottom ice slab interface. Additional
heterogeneities at depth, such as interstitial firn or variations in the ice slab thickness, could also contribute to P_c variability.
The integration of reflections from these heterogeneities within the HiCARS/MARFA range resolution could drive large
fluctuations in P_c behavior due to constructive/destructive interferences. This would explain the higher IQRs observed in
Zone II by HiCARS/MARFA compared to MCoRDS. However, we note a region Zone IIb within Zone II (Fig. 3b), where
285 anomalously strong P_c values from MARFA are observed. P_c within Zone IIb behaves similarly to P_c in Zones I and III,
suggesting the presence of either relatively homogeneous firn or compact glacier ice. Zone IIb could alternatively feature
interstitial firn in an ice slab resulting in higher P_c values relative to its surroundings, as similarly observed from 25 to 28 km
along the GPR radargram (Fig. 2). Additionally, the P_c/P_n ratio approximately equals 0 dB in Zone IIb and appears distinct
from the other three zones (Fig. S4). This subzonal region may represent a new firn zone with inclusions that equally scatters
290 and reflects the radar return but less heterogeneous than the surrounding Zone II.

The finer range resolution of MCoRDS limits P_c sensitivity to the firn$_1$ layer and partially the ice slab. Any changes in firn
structure at depths beyond the MCoRDS range resolution are not captured by P_c. We interpret P_c from MCoRDS in Zone II
to be sensitive to layers consisting primarily of thin ice lenses embedded within the firn$_1$ layer and the top ice slab interface,
295 all expected to generate coherent reflections. The depth of the top ice slab interface changes little relative to the bottom
interface (Rutishauser et al., 2016). Due to limited firn heterogeneities and variations in firn structure within the range
resolution of MCoRDS, there is less observed variability in P_c from MCoRDS in Zone II. Thus, the Zone II near-surface
appears spatially and vertically homogeneous to MCoRDS, consistent with the similar pattern of high P_c values in Zone I.

The Cryosphere
Discussions

3.2.4 Zone III: compact glacier ice

300   The pattern of P_c from MCoRDS is noticeably different in Zone III compared to that of Zones I and II (Fig. 3c), where P_c from MCoRDS is generally lower in Zone III (<10 dB) compared to Zones I and II (≥10 dB). Where this pattern shift occurs coincides with the Zone II/Zone III boundary defined using only MARFA data, thus further validating this approach for delineating zones. Interzonal comparison of P_c by IPR survey indicates greater variability in Zone III compared to the other two zones (Fig. 4), suggesting another change in the near-surface structure of Zone III that likely affects the return from all

305   IPRs. Intrazonally, IQRs within Zone III are dissimilar when compared to each other, which further suggests that the near-surface structure affects each IPR's surface return in different ways. Zone III consists mainly of compact glacier ice without firn and theoretically should produce a strong and stable coherent return. The fact that we do not observe this behavior throughout all of Zone III indicates the near-surface structure appears spatially and vertically heterogeneous for all three IPRs.

310

While P_c is challenging to interpret in Zone III, the dual-frequency IPR approach can provide insight to possibly explain these observed variations. For example, we investigate how the snow cover alone in Zone III, prior to the onset of the melt season, might influence P_c at the two frequencies of interest. Spring snow depth measurements on DIC indicate the snow layer thickness can vary tens of centimeters, increasing from northwest (<50 cm) to southeast (>100 cm) across the ice cap

315   (Koerner, 1966). To study the effects of such a layer, we model its reflectivity embedded in between semi-infinite half spaces of air above and compact ice below, as a function of snow layer thickness and permittivity (Fig. S5). For typical snow densities (equivalent to $\varepsilon \leq 1.7$), reflectivity is found to only vary by several dB for most snow layer thicknesses. Exceptions occur when ε approaches ~1.7 or fairly dense snow at specific layer thicknesses (Fig. S5). To generate the P_c variability observed by both frequencies in Zone III, a ~90 cm thick snow cover with centimeter scale thickness variability and $\varepsilon \approx 1.7$

320   would be required throughout this zone. This scenario is inconsistent with spring snowpack thicknesses across DIC (Koerner, 1966) and thus cannot fully account for P_c variations in Zone III.

An alternative hypothesis may involve remnant supraglacial river channels carved during the previous melt season (see Discussion). These channelized features vary spatially across Zone III (Fig. 5) and may retain their structure when refrozen

325   and buried underneath the winter snowpack. These snow-filled, lineated structures may induce non-negligible effects on P_c, as a result of surface roughness and snow depth variability. Further analysis to test this hypothesis, while insightful, remains out of scope for this work.

4 Discussion
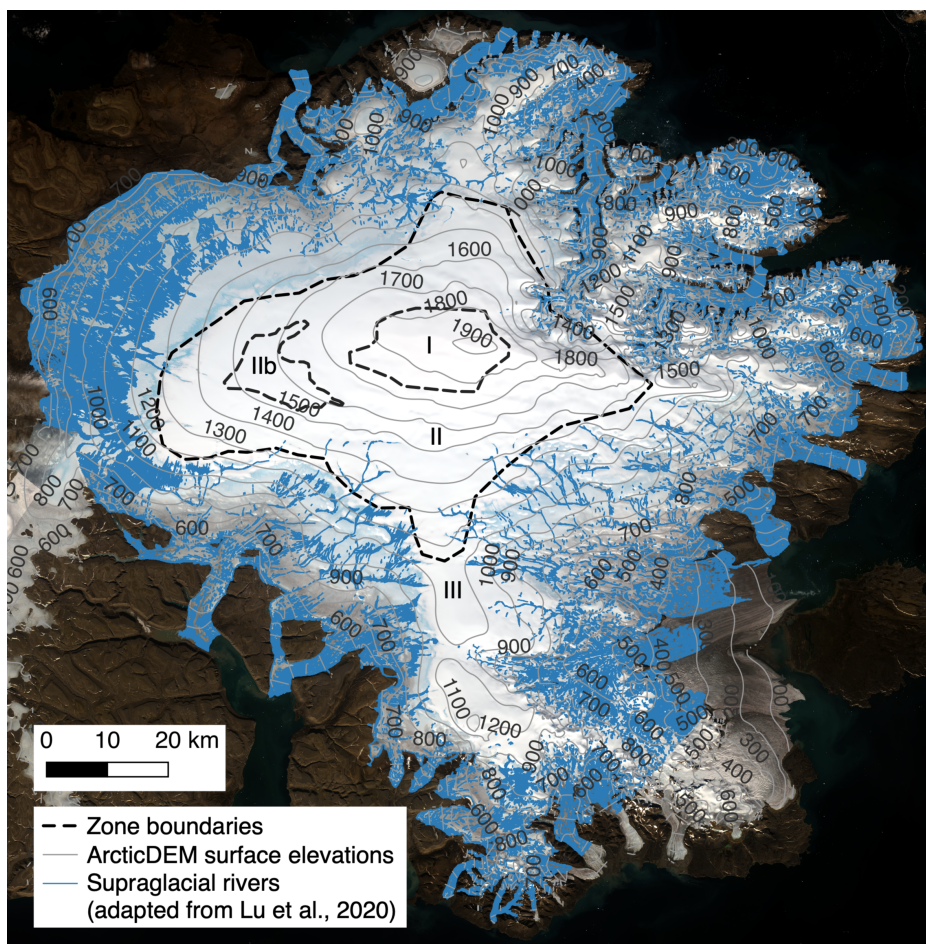
Figure 5. Landsat-8 images (courtesy of the U.S. Geological Survey) of Devon Ice Cap taken mid-August 2019, overlain with zone boundaries derived from MARFA and supraglacial rivers previously mapped by Lu et al. (2020).

Our results along with those of Lu et al. (2020) indicate the DIC near-surface firn may exhibit conditions that favor lateral runoff over vertical infiltration of surface meltwater in certain regions across the ice cap. The thickness of ice slabs within Zone II affects the bulk firn permeability and thus the capability of vertical meltwater infiltration. Based on differences between the range resolutions of IPRs in this study, we can estimate the average thickness of ice slabs in Zone II. Because MCoRDS is expected to only capture the upper interface of the ice slab while HiCARS/MARFA captures its entirety, the difference between their range resolutions provides an estimate of average ice slab thickness (h), calculated as

$$h \approx z_{0,mix,HiCARS/MARFA} - z_{0,mix,MCoRDS} \text{,} \tag{5}$$

where $z_{0,mix,IPR}$ is the range resolution of an IPR system associated with a heterogeneous medium/mixture of ε_{eff} defined by Eq. (1). While usually unknown, ε_{eff} for a mixture composed of firn and ice (e.g., an ice slab in firn) is expected to be bounded by the permittivity of their end member components. Based on Eq. (1), $z_{0,mix,IPR}$ is then also expected to be bounded by the range resolutions defined for a homogeneous medium of either firn ($z_{0,firn,IPR}$) or ice ($z_{0,ice,IPR}$). This

345 implies that the difference between the range resolutions of HiCARS/MARFA and MCoRDS when probing a homogeneous medium of firn or ice yields a range of average ice slab thicknesses, such that $(z_{0,ice,HiCARS/MARFA} - z_{0,ice,MCoRDS}) < h < (z_{0,firn,HiCARS/MARFA} - z_{0,firn,MCoRDS})$. From this, we estimate average ice slab thicknesses range from 4.2 to 5.6 m in Zone II on DIC, based on values provided in Table 1. These estimates are consistent with GPR profiles, particularly at lower elevations within Zone II (Gascon et al., 2013; Rutishauser et al., 2016).

350

Our ice slab thicknesses are thicker than the impermeable thickness threshold of at least 1 m noted by Ashmore et al. (2020) and overall similar to the observed thickness of Greenland's ice slabs, which can limit or substantially delay meltwater percolation (Charalampidis et al., 2016; Machguth et al., 2016; MacFerrin et al., 2019). Spatially, the radar response associated with refrozen ice slabs in Zone II is widespread (Fig. 3), suggesting impermeable ice slabs are most likely

355 ubiquitous and continuous in Zone II except in the anomalous subzonal region, Zone IIb. Here, discontinuous thin ice lenses could be present instead, similar to Zone I as opposed to the compact glacier ice of Zone III, since firn is present at these elevations (Fig. 5). Additional data (e.g., firn cores and GPR) would help characterize the firn properties of Zone IIb.

Given the hypothesized thickness and continuity of ice slabs in DIC, we find that the near-surface structure of Zone II could

360 enable lateral meltwater runoff atop ice slabs through the firn₁ layer. However, it is uncertain as to whether some of this meltwater would refreeze within the firn during lateral runoff. Any latent heat released from refreezing would raise firn temperatures and promote subsequent meltwater runoff, due to the lack of sufficient cold content that would otherwise facilitate refreezing (Vandecrux et al., 2020a). The firn₁ layer is relatively thin (~1 m) and can experience seasonal temperature fluctuations through conduction with the atmosphere. Therefore, during the melt season, atmospheric warming

365 could also raise firn temperatures and promote lateral runoff. The extent to which runoff occurs depends on the balance between the volume of surface meltwater produced and the available firn storage capacity in each basin, which is modulated by the thermal and hydraulic properties of the firn that control infiltration and refreezing.

In Zone III, Lu et al. (2020) mapped seasonal supraglacial river networks on DIC from imagery collected in 2016, where

370 some rivers appear to form in Zone II (Fig. 5). This suggests that the firn stratigraphy likely influences the development of supraglacial meltwater channels. We hypothesize that high-elevation surface meltwater runoff over ice slabs in Zone II may contribute to the total meltwater supply routed through supraglacial rivers in the ablation zone. If enough meltwater is produced and saturates the firn, then slush flows could also develop (Fernandes et al., 2018; Pitcher and Smith, 2019),

particularly near the Zone II/III boundary. The development of both dendritic and parallel supraglacial river networks observed on DIC (Lu et al., 2020) might imply how meltwater is routed through preferred pathways through the overlying firn. Future studies of the Zone II firn structure may reveal how it could modulate water fluxes at the accumulation/ablation zone boundary that could drive some of the observed but unexplained variations in the channel structure in the upper ablation zone. Because the Zone II/III boundary tracks the visible runoff line depicted by LandSat-8 imagery (Fig. 5), repeat IPR surveys of DIC would capture shifts in the Zone II/III boundary over time that may correspond to spatial shifts in physical properties controlling runoff.

A lack of supraglacial rivers extending upslope into Zone II is observed in northwest DIC (Fig. 5). This could be attributed to where rivers had not fully developed during the melt season when mapped by Lu et al. (2020). While the full mapping of supraglacial rivers used images taken in late July, Lu et al. (2020) also found that rivers in certain regions extend to higher elevations later into the melt season. This includes western DIC, where rivers develop at higher elevations between 1400 to 1500 m in mid-August (Lu et al., 2020), coinciding with the Zone II/III boundary and corresponding to when the LandSat-8 images were captured (Fig. 5). The relatively shallow slopes of northwest DIC may influence the rate at which rivers form compared to other regions across the ice cap. In addition, the 10 m resolution of images used by Lu et al. (2020) could have prevented detection of relatively narrow streams that otherwise are present.

Although inverting P_c for the bulk density is challenging due to the nonuniqueness of reflectivity as a function of layer thickness, analyzing the character of P_c from dual-frequency IPR, in combination with P_n (Rutishauser et al., 2016), can still provide insight into the presence of near-surface layering when lacking data from GPR, firn cores, or higher frequency airborne radar sounders. Thus, in regions dominated by significant surface melting and refreezing processes in firn, we caution the inversion of P_c for surface density similar to previous applications of RSR (Grima et al., 2014b, 2016). Having dual-frequency IPR observations would help confirm whether P_c is representative of surface density, because P_c from both frequencies/bandwidths would be expected to be the same in a firn column without layering.

5 Conclusion

Our results indicate that the surface coherent power derived from RSR is sensitive to bulk firn properties featuring ice layers embedded in firn. Modeled reflectivity values visually correlate well with the observed coherent power on DIC, based on the stack configuration that best describes the near-surface structure of the corresponding zone. Together with Rutishauser et al. (2016), we present the first study aimed to characterize the vertical and spatial extent of ice layers in firn over an entire ice cap with dual-frequency IPR. We demonstrate how each system captures near-surface heterogeneity to different vertical extents, limited by their bandwidth-constrained range resolutions. We leverage these differences in range resolution to constrain the thickness of ice slabs within Zone II. Our thickness estimates imply that ice slabs are impermeable and thus

17

capable of impeding vertical meltwater percolation in favor of lateral runoff in Zone II. Ice slabs are likely pervasive, which suggests that lateral flow may dominate over deep percolation and local retention in Zone II and feed supraglacial rivers downslope. Coupled with warming temperatures (Mortimer et al., 2016), we predict that the DIC near-surface will continue to promote surface meltwater runoff if such conditions are sustained.

410

The DIC is well suited for studying the mechanisms that control firn hydrology, with applications to other regions experiencing significant surface melting such as Greenland. Such studies could help validate results from multidimensional firn models, in order to accurately capture complex heterogeneous meltwater percolation and refreezing in firn (Vandecrux et al., 2020b). In addition, our study demonstrates quantitatively the first proof of concept for using a dual frequency approach

415 to characterize the near-surface of extraterrestrial environments. Such an approach is applicable to where dual-frequency IPR data already exists, such as on Mars, or will be collected at Jupiter's moon Europa. Future exploration with the dual-frequency radar sounder onboard NASA's Europa Clipper mission can apply a similar approach to detect and characterize near-surface ice layers and overburden. Unlike on Earth, ice layers may form from hypothesized brine infiltration and refreeze in icy regolith on Europa (Chan et al., 2017; Schmidt et al., 2011), thus identifying locations of potential near-

420 surface endogenic activity.

Data Availability

We are currently preparing data used in this study for publication, if not already publicly available.

Author Contributions

KC, CG, AR, and DDB conceptualized the study. KC developed the model, led the data visualization, and wrote the
425 manuscript. AR collected and processed the GPR and firn core data. DAY processed and curated the HiCARS and MARFA datasets. CG derived the RSR products for the HiCARS and MARFA datasets. RC derived the RSR products for the MCoRDS dataset. KC, CG, AR, RC, and DDB contributed to data analysis and interpretation. DDB acquired funding for this study. All authors reviewed and edited the manuscript.

Competing Interests

430 The authors declare that they have no conflict of interest.

The Cryosphere
Discussions
EGU Open Access

References

Arnold, E., Rodriguez-Morales, F., Paden, J., Leuschen, C., Keshmiri, S., Yan, S., Ewing, M., Hale, R., Mahmood, A., Blevins, A., Mishra, A., Karidi, T., Miller, B., and Sonntag, J.: HF/VHF Radar Sounding of Ice from Manned and Unmanned Airborne Platforms, Geosciences, 8, 182, https://doi.org/10.3390/geosciences8050182, 2018.

Arnold, E., Leuschen, C., Rodriguez-Morales, F., Li, J., Paden, J., Hale, R., and Keshmiri, S.: CReSIS airborne radars and platforms for ice and snow sounding, Annals of Glaciology, 1–10, https://doi.org/10.1017/aog.2019.37, 2019.

Ashmore, D. W., Mair, D. W. F., and Burgess, D. O.: Meltwater percolation, impermeable layer formation and runoff buffering on Devon Ice Cap, Canada, J. Glaciol., 66, 61–73, https://doi.org/10.1017/jog.2019.80, 2020.

Bell, C., Mair, D., Burgess, D., Sharp, M., Demuth, M., Cawkwell, F., Bingham, R., and Wadham, J.: Spatial and temporal variability in the snowpack of a High Arctic ice cap: implications for mass-change measurements, Annals of Glaciology, 48, 159–170, https://doi.org/10.3189/172756408784700725, 2008.

Bezeau, P., Sharp, M., Burgess, D., and Gascon, G.: Firn profile changes in response to extreme 21st-century melting at Devon Ice Cap, Nunavut, Canada, Journal of Glaciology, 59, 981–991, https://doi.org/10.3189/2013JoG12J208, 2013.

Born, M. and Wolf, E.: Principles of optics; electromagnetic theory of propagation, interference and diffraction of light, 4th ed., Pergamon Press, Oxford, 1970.

van den Broeke, M. R., Enderlin, E. M., Howat, I. M., Kuipers Munneke, P., Noël, B. P. Y., van de Berg, W. J., van Meijgaard, E., and Wouters, B.: On the recent contribution of the Greenland ice sheet to sea level change, The Cryosphere, 10, 1933–1946, https://doi.org/10.5194/tc-10-1933-2016, 2016.

Cavitte, M. G. P., Young, D. A., Mulvaney, R., Ritz, C., Greenbaum, J. S., Ng, G., Kempf, S. D., Quartini, E., Muldoon, G. R., Paden, J., Frezzotti, M., Roberts, J. L., Tozer, C. R., Schroeder, D. M., and Blankenship, D. D.: A detailed radiostratigraphic data set for the central East Antarctic Plateau spanning from the Holocene to the mid-Pleistocene, Earth System Science Data, 13, 4759–4777, https://doi.org/10.5194/essd-13-4759-2021, 2021.

The Cryosphere
Discussions

Open Access

EGU

Chan, K.: Mapping ice in firn with airborne ice-penetrating radar, Nat Rev Earth Environ, 3, 291–291,
465   https://doi.org/10.1038/s43017-022-00290-z, 2022.

Chan, K., Grima, C., Blankenship, D. D., Young, D. A., and Soderlund, K. M.: Mobilization of Near-Surface Brine on
Europa, in: Europa Deep Dive 1: Ice-Shell Exchange Processes, Europa Deep Dive 1: Ice-Shell Exchange Processes, 7014,
2017.

Charalampidis, C., As, D. V., Colgan, W. T., Fausto, R. S., Macferrin, M., and Machguth, H.: Thermal tracing of retained
470   meltwater in the lower accumulation area of the Southwestern Greenland ice sheet, Annals of Glaciology, 57, 1–10,
https://doi.org/10.1017/aog.2016.2, 2016.

CReSIS: CReSIS Radar Depth Sounder Data, https://data.cresis.ku.edu/data/rds/rds_readme.pdf, 2016.

Culberg, R., Schroeder, D. M., and Chu, W.: Extreme melt season ice layers reduce firn permeability across Greenland, Nat
Commun, 12, 2336, https://doi.org/10.1038/s41467-021-22656-5, 2021.

475   Fernandes, L., Schmitt, A., Wendleder, A., Sharp, M., and Roth, A.: Detecting Supraglacial Meltwater Drainage on the
Devon Ice Cap using Kennaugh Decomposition of TerraSAR-X imagery, in: EUSAR 2018; 12th European Conference on
Synthetic Aperture Radar, EUSAR 2018; 12th European Conference on Synthetic Aperture Radar, 1–6, 2018.

Forster, R. R., Box, J. E., van den Broeke, M. R., Miège, C., Burgess, E. W., van Angelen, J. H., Lenaerts, J. T. M., Koenig,
L. S., Paden, J., Lewis, C., Gogineni, S. P., Leuschen, C., and McConnell, J. R.: Extensive liquid meltwater storage in firn
480   within the Greenland ice sheet, Nature Geosci, 7, 95–98, https://doi.org/10.1038/ngeo2043, 2014.

Fujita, S., Matsuoka, T., Ishida, T., Matsuoka, K., and Mae, S.: A summary of the complex dielectric permittivity of ice in
the megahertz range and its applications for radar sounding of polar ice sheets, 29, 2000.

Gascon, G., Sharp, M., Burgess, D., Bezeau, P., and Bush, A. B. G.: Changes in accumulation-area firn stratigraphy and
meltwater flow during a period of climate warming: Devon Ice Cap, Nunavut, Canada, J. Geophys. Res. Earth Surf., 118,
485   2380–2391, https://doi.org/10.1002/2013JF002838, 2013.

Gascon, G., Sharp, M., Burgess, D., Bezeau, P., Bush, A. B. G., Morin, S., and Lafaysse, M.: How well is firn densification
represented by a physically based multilayer model? Model evaluation for Devon Ice Cap, Nunavut, Canada, J. Glaciol., 60,
694–704, https://doi.org/10.3189/2014JoG13J209, 2014.

Grima, C., Kofman, W., Herique, A., Orosei, R., and Seu, R.: Quantitative analysis of Mars surface radar reflectivity at
490   20MHz, Icarus, 220, 84–99, https://doi.org/10.1016/j.icarus.2012.04.017, 2012.

Grima, C., Schroeder, D. M., Blankenship, D. D., and Young, D. A.: Planetary landing-zone reconnaissance using ice-
penetrating radar data: Concept validation in Antarctica, Planetary and Space Science, 103, 191–204,
https://doi.org/10.1016/j.pss.2014.07.018, 2014a.

Grima, C., Blankenship, D. D., Young, D. A., and Schroeder, D. M.: Surface slope control on firn density at Thwaites
495   Glacier, West Antarctica: Results from airborne radar sounding, Geophys. Res. Lett., 41, 6787–6794,
https://doi.org/10.1002/2014GL061635, 2014b.

Grima, C., Greenbaum, J. S., Lopez Garcia, E. J., Soderlund, K. M., Rosales, A., Blankenship, D. D., and Young, D. A.:
Radar detection of the brine extent at McMurdo Ice Shelf, Antarctica, and its control by snow accumulation, Geophys. Res.
Lett., 43, 7011–7018, https://doi.org/10.1002/2016GL069524, 2016.

500   Grima, C., Koch, I., Greenbaum, J. S., Soderlund, K. M., Blankenship, D. D., Young, D. A., Schroeder, D. M., and Fitzsimons, S.: Surface and basal boundary conditions at the Southern McMurdo and Ross Ice Shelves, Antarctica, Journal of Glaciology, 65, 675–688, https://doi.org/10.1017/jog.2019.44, 2019.

Koerner, R. M.: Accumulation on the Devon Island Ice Cap, Northwest Territories, Canada, Journal of Glaciology, 6, 383–392, https://doi.org/10.3189/S0022143000019493, 1966.

505   Kovacs, A., Gow, A. J., and Morey, R. M.: The in-situ dielectric constant of polar firn revisited, Cold Regions Science and Technology, 23, 245–256, https://doi.org/10.1016/0165-232X(94)00016-Q, 1995.

Lu, Y., Yang, K., Lu, X., Smith, L. C., Sole, A. J., Livingstone, S. J., Fettweis, X., and Li, M.: Diverse supraglacial drainage patterns on the Devon ice Cap, Arctic Canada, Journal of Maps, 16, 834–846, https://doi.org/10.1080/17445647.2020.1838353, 2020.

510   MacFerrin, M., Machguth, H., As, D. van, Charalampidis, C., Stevens, C. M., Heilig, A., Vandecrux, B., Langen, P. L., Mottram, R., Fettweis, X., Broeke, M. R. van den, Pfeffer, W. T., Moussavi, M. S., and Abdalati, W.: Rapid expansion of Greenland's low-permeability ice slabs, Nature, 573, 403–407, https://doi.org/10.1038/s41586-019-1550-3, 2019.

MacGregor, J. A., Boisvert, L. N., Medley, B., Petty, A. A., Harbeck, J. P., Bell, R. E., Blair, J. B., Blanchard-Wrigglesworth, E., Buckley, E. M., Christoffersen, M. S., Cochran, J. R., Csathó, B. M., De Marco, E. L., Dominguez, R. T.,
515   Fahnestock, M. A., Farrell, S. L., Gogineni, S. P., Greenbaum, J. S., Hansen, C. M., Hofton, M. A., Holt, J. W., Jezek, K. C., Koenig, L. S., Kurtz, N. T., Kwok, R., Larsen, C. F., Leuschen, C. J., Locke, C. D., Manizade, S. S., Martin, S., Neumann, T. A., Nowicki, S. M. J., Paden, J. D., Richter-Menge, J. A., Rignot, E. J., Rodríguez-Morales, F., Siegfried, M. R., Smith, B. E., Sonntag, J. G., Studinger, M., Tinto, K. J., Truffer, M., Wagner, T. P., Woods, J. E., Young, D. A., and Yungel, J. K.: The Scientific Legacy of NASA's Operation IceBridge, Reviews of Geophysics, 59, e2020RG000712,
520   https://doi.org/10.1029/2020RG000712, 2021.

Machguth, H., MacFerrin, M., van As, D., Box, J. E., Charalampidis, C., Colgan, W., Fausto, R. S., Meijer, H. A. J., Mosley-Thompson, E., and van de Wal, R. S. W.: Greenland meltwater storage in firn limited by near-surface ice formation, Nature Clim Change, 6, 390–393, https://doi.org/10.1038/nclimate2899, 2016.

Mortimer, C. A., Sharp, M., and Wouters, B.: Glacier surface temperatures in the Canadian High Arctic, 2000–15, J.
525   Glaciol., 62, 963–975, https://doi.org/10.1017/jog.2016.80, 2016.

Mouginot, J., Kofman, W., Safaeinili, A., Grima, C., Herique, A., and Plaut, J. J.: MARSIS surface reflectivity of the south residual cap of Mars, Icarus, 201, 454–459, https://doi.org/10.1016/j.icarus.2009.01.009, 2009.

Peters, M. E., Blankenship, D. D., Carter, S. P., Kempf, S. D., Young, D. A., and Holt, J. W.: Along-Track Focusing of Airborne Radar Sounding Data From West Antarctica for Improving Basal Reflection Analysis and Layer Detection, IEEE
530   Trans. Geosci. Remote Sensing, 45, 2725–2736, https://doi.org/10.1109/TGRS.2007.897416, 2007.

Pettinelli, E., Cosciotti, B., Di Paolo, F., Lauro, S. E., Mattei, E., Orosei, R., and Vannaroni, G.: Dielectric properties of Jovian satellite ice analogs for subsurface radar exploration: A review, Rev. Geophys., 53, 593–641, https://doi.org/10.1002/2014RG000463, 2015.

Pitcher, L. H. and Smith, L. C.: Supraglacial Streams and Rivers, Annual Review of Earth and Planetary Sciences, 47, 421–
535   452, https://doi.org/10.1146/annurev-earth-053018-060212, 2019.

Rodriguez-Morales, F., Gogineni, S., Leuschen, C. J., Paden, J. D., Li, J., Lewis, C. C., Panzer, B., Gomez-Garcia Alvestegui, D., Patel, A., Byers, K., Crowe, R., Player, K., Hale, R. D., Arnold, E. J., Smith, L., Gifford, C. M., Braaten, D.,

and Panton, C.: Advanced Multifrequency Radar Instrumentation for Polar Research, IEEE Transactions on Geoscience and Remote Sensing, 52, 2824–2842, https://doi.org/10.1109/TGRS.2013.2266415, 2014.

540   Rutishauser, A., Grima, C., Sharp, M., Blankenship, D. D., Young, D. A., Cawkwell, F., and Dowdeswell, J. A.: Characterizing near-surface firn using the scattered signal component of the glacier surface return from airborne radio-echo sounding: Characterizing Firn via Radar Scattering, Geophys. Res. Lett., 43, 12,502-12,510, https://doi.org/10.1002/2016GL071230, 2016.

Rutishauser, A., Blankenship, D. D., Sharp, M., Skidmore, M. L., Greenbaum, J. S., Grima, C., Schroeder, D. M.,
545   Dowdeswell, J. A., and Young, D. A.: Discovery of a hypersaline subglacial lake complex beneath Devon Ice Cap, Canadian Arctic, Sci. Adv., 4, eaar4353, https://doi.org/10.1126/sciadv.aar4353, 2018.

Rutishauser, A., Blankenship, D. D., Young, D. A., Wolfenbarger, N. S., Beem, L. H., Skidmore, M. L., Dubnick, A., and Criscitiello, A. S.: Radar sounding survey over Devon Ice Cap indicates the potential for a diverse hypersaline subglacial hydrological environment, The Cryosphere, 16, 379–395, https://doi.org/10.5194/tc-16-379-2022, 2022.

550   Scanlan, K. M., Rutishauser, A., Young, D. A., and Blankenship, D. D.: Interferometric discrimination of cross-track bed clutter in ice-penetrating radar sounding data, Ann. Glaciol., 61, 68–73, https://doi.org/10.1017/aog.2020.20, 2020.

Schmidt, B. E., Blankenship, D. D., Patterson, G. W., and Schenk, P. M.: Active formation of 'chaos terrain' over shallow subsurface water on Europa, Nature, 479, 502–505, https://doi.org/10.1038/nature10608, 2011.

Sihvola, A. H.: Electromagnetic Mixing Formulas and Applications, IET, 326 pp., 1999.

555   Sylvestre, T., Copland, L., Demuth, M. N., and Sharp, M.: Spatial patterns of snow accumulation across Belcher Glacier, Devon Ice Cap, Nunavut, Canada, J. Glaciol., 59, 874–882, https://doi.org/10.3189/2013JoG12J227, 2013.

Trusel, L. D., Das, S. B., Osman, M. B., Evans, M. J., Smith, B. E., Fettweis, X., McConnell, J. R., Noël, B. P. Y., and van den Broeke, M. R.: Nonlinear rise in Greenland runoff in response to post-industrial Arctic warming, Nature, 564, 104–108, https://doi.org/10.1038/s41586-018-0752-4, 2018.

560   Ulaby, F. T., Moore, R. K., and Fung, A. K.: Microwave remote sensing: Active and passive. Volume 1 - Microwave remote sensing fundamentals and radiometry, 1981.

Vandecrux, B., Fausto, R. S., As, D. van, Colgan, W., Langen, P. L., Haubner, K., Ingeman-Nielsen, T., Heilig, A., Stevens, C. M., MacFerrin, M., Niwano, M., Steffen, K., and Box, J. E.: Firn cold content evolution at nine sites on the Greenland ice sheet between 1998 and 2017, Journal of Glaciology, 66, 591–602, https://doi.org/10.1017/jog.2020.30, 2020a.

565   Vandecrux, B., Mottram, R., Langen, P. L., Fausto, R. S., Olesen, M., Stevens, C. M., Verjans, V., Leeson, A., Ligtenberg, S., Kuipers Munneke, P., Marchenko, S., van Pelt, W., Meyer, C. R., Simonsen, S. B., Heilig, A., Samimi, S., Marshall, S., Machguth, H., MacFerrin, M., Niwano, M., Miller, O., Voss, C. I., and Box, J. E.: The firn meltwater Retention Model Intercomparison Project (RetMIP): evaluation of nine firn models at four weather station sites on the Greenland ice sheet, The Cryosphere, 14, 3785–3810, https://doi.org/10.5194/tc-14-3785-2020, 2020b.

570